Nanoscale Defect Formation on InP(111) Surfaces after MeV Sb Implantation

Dipak Paramanik¹, Asima Pradhan², and Shikha Varma^{1,*}

¹Institute of Physics, Bhubaneswar - 751005, India. ²Department of Physics, IIT, Kanpur - 208016, India

Abstract

We have studied the surface modifications as well as the surface roughness of the InP(111) surfaces after 1.5 MeV Sb ion implantations. Scanning Probe Microscope (SPM) has been utilized to investigate the ion implanted InP(111) surfaces. We observe the formation of nanoscale defect structures on the InP surface. The density, height and size of the nanostructures have been investigated here as a function of ion fluence. The rms surface roughness, of the ion implanted InP surfaces, demonstrates two varied behaviors as a function of Sb ion fluence. Initially, the roughness increases with increasing fluence. However, after a critical fluence the roughness decreases with increasing fluence. We have further applied the technique of Raman scattering to investigate the implantation induced modifications and disorder in InP. Raman Scattering results demonstrate that at the critical fluence, where the decrease in surface roughness occurs, InP lattice becomes amorphous.

^{*} Corresponding author: shikha@iopb.res.in; Tel:91-674-2301058; FAX:91-674-2300142

1 Introduction

InP is progressively being considered as a potential candidate for high speed electronic devices and opto electronic applications [1, 2, 3]. Sb is also considered an important dopant because of its role in the development of field effect transistors and infrared detectors [4]. Due to its excellent physical properties like high thermal conductivity, high peak velocities for electrons and holes, InP is considered an important semiconductor material and it is being prominently utilized in the devices for high electron mobility transistors, high efficiency and high speed quantum well lasers, photo-detectors, photonic integrated circuits etc. Although InP is being extensively used in semiconductor based device technology, it has been investigated much less compared to GaAs. Due to its low thermal stability, MeV ion implantation is a prominent way to introduce and dope the materials in InP. MeV implantation is also important for forming thick buried layers with modified properties as well as modification of vertically limited layers and quantum well structures. The increased density in VLSI circuits also makes the technological applications of the ion implantation, especially in MeV energy range, increasingly important. MeV implantation however can also produce severe modifications in the material depending on the nature and the energy of the impinging ion, and the implantation dose [5]. Extensive usage of ion implantation in device fabrication and the continued miniaturization of device structures has brought the issue of surface modifications, via ion implantations, to the forefront. However, the factors responsible for such modifications and the surface morphology after ion implantation, have received little attention [6]. Since roughness of surface can crucially effect the performance and reliability of devices [7], it becomes necessary to characterize the surface roughness and understand the processes influencing it. The formation and the development of the surface structures, due to the ion implantation, are also gaining importance because of the realization that

these structures can be utilized for controlled fabrication of semiconductors similar to self-organized growths.

Scanning Probe microscope (SPM) is a very effective tool for examining surface modifications and surface structures. There are very few studies in literature that have investigated the morphological changes of the ion implanted InP surfaces by SPM. Moreover, the surface studies on InP surfaces have been performed either after keV implantations [8] or after Swift Heavy Ion (SHI) irradiations at several hundreds of MeV [9, 10], and there are no surface studies in literature where MeV implantations on InP have been investigated. In the present study we have made a detailed investigation on InP(111) surfaces after 1.5 MeV Sb implantation.

During implantation, a projectile while moving forward produces defects and loses energy due to scattering processes. The ion gets finally deposited at the range governed by its mass and implant energy [11]. At MeV energies, nuclear energy loss (S_n) processes are expected to be dominantly responsible for the material modifications. Defects and strains can get produced, via S_n , causing the modifications in the surface and bulk properties [12, 13]. Raman scattering intensity and peak shifts of the zone center phonon peak are very sensitive to these modifications. Formation of defects can also lead to stress in the planes of the single crystal as well as changes in force constants. Corresponding shifts in the phonon frequencies are reflected in the Raman spectra. Our earlier study of MeV implantation in Si [14] had shown that the Raman scattering is a powerful technique for investigating and monitoring the implantation induced modifications. It has also been shown to be a very sensitive probe for small volume defects created in Si during ion implantation [14, 15, 16]. Cusco et.al. have utilized Raman Spectroscopy to investigate the fluence dependant keV implantation of Si⁺ in InP(100) [17]. Defect annealing after 2 MeV Yb⁺ implantation, for a single fluence of $1 \times 10^{13} cm^{-2}$ in InP(100) has also been investigated by Raman spectroscopy

[18]. In the present study, in addition to SPM, we have also utilized Raman scattering technique to investigate the fluence dependant modifications in InP after 1.5 MeV Sb implantation. Moreover, the crystalline/amorphous phase transition of InP for high Sb fluences has also been observed here through Raman scattering.

In this paper we have utilized the SPM technique to understand the modification in roughness and morphology of InP surfaces upon 1.5 MeV Sb ion implantation. Formation of nanoscale defect structures on InP surface due to Sb implantation have been observed in SPM images. The height and size distributions of the nanoscale defect structures have been presented here. We further observe that the MeV Sb ion implantation in InP leads to surface roughness that displays two different behaviours as a function of fluence. Initially, the surface roughness increases with increasing fluence. Beyond a critical fluence, however, the surface roughness decreases with increasing fluence. We have utilized the Raman scattering results to understand the modifications in surface roughness of InP after implantation. The Raman scattering results indicate that the critical fluence, where the surface roughness begins to decrease for increasing fluence, occurs at a stage when the InP lattice has become amorphous. The smoothening of the surface thus may be related to the amorphization in InP. Our results here are different than those observed after 100 MeV Au SHI (Swift Heavy ion) irradiation [10] of InP(111) where, compared to our results, a lower rms surface roughness below $1\times10^{13}ions/cm^2$ but a higher roughness for larger fluences was observed.

Experimental procedures are discussed in section 2. Nanoscale defect formation on surfaces, rms surface roughness and Raman Scattering studies of InP(111) after implantation are presented in section 3. Conclusions are presented in section 4.

2 Experimental

A mirror polished (111)-oriented InP single crystal wafer was used in the present study. The samples were implanted at room temperature with a scanned beam of 1.5 MeV Sb²⁺ ions at various fluences ranging from 1×10^{11} to $5\times10^{15}ions/cm^2$. The average Sb flux was $0.02~\mu\text{A/cm}^2$. This current was measured directly on the target after suppressing the secondary electrons by applying a negative bias of 200V to a suppressor assembly around the target. The implantations were performed with the samples oriented 7^o off-normal to the incident beam to avoid channeling effects. Monte Carlo simulations were performed for 1.5 MeV Sb implantation in InP using the SRIM'03 code and the mean projected range of Sb-ion distribution was found to be 400 nm [19].

Scanning Probe Microscope (SPM) Nanoscope IIIA from Veeco was used to image the implanted InP (111) sample surfaces with a silicon nitride cantilever operated in tapping mode. Images ranging from 0.2 to 10 μm square were obtained. The root mean square (rms) surface roughness was calculated by the SPM software.

Raman scattering measurements were performed using a SPEX 1877E Triplemate Spectrometer with a liquid nitrogen cooled, charged coupled device array. The laser power was controlled to avoid laser annealing effect on the sample. Raman experiments were carried out at room temperature using the 514 nm line of an Argon ion laser in the backscattering geometry. At this wavelength the penetration depth of the light is estimated to be about 100 nm. As the penetration depth of the light is much smaller than the projected range of the implanted Sb ions, Raman scattering results are primarily from the surface region.

3 Results and Discussion

Fig.1 shows the $10\times10\mu m^2$ 2D SPM images from the InP surfaces. The image from a virgin (un-implanted) InP(111) sample is shown and it is observed that this surface is smooth. Other images of Fig. 1 show the evolution of the surface morphology on InP surfaces after 1.5 MeV Sb implantation at fluences ranging from $1\times10^{11}ions/cm^2$ to $1 \times 10^{15} ions/cm^2$. Comparison of the surface morphologies of InP surfaces of Fig. 1, after implantation, show the formation of nanoscale sized defects with varying size, height and density depending on the fluence. Fig.1a shows the InP surface after an Sb implantation with $1\times10^{11}ions/cm^2$. Several nano sized defects can be observed on the surface. The structures have developed due to the damage created at the surface. Some surface structures have been earlier reported after keV Ar ion irradiation of InP surfaces [8] and 4.5 MeV Au implantation on HOPG surfaces [20]. Nanoscale defects on InP surfaces have also been observed after 100 MeV Au SHI irradiations [21]. However, the present study is the first study of modifications of InP surfaces after MeV implantation. We have investigated the height and the size distribution of the nanoscale sized defects (seen in Fig. 1) on the InP surfaces after various Sb fluences. The size and the height distributions are shown in Fig.2 and 3 respectively. After a fluence of $1\times10^{11}ions/cm^2$, most of the nanostructures have a diameter smaller than 450 nm and a height smaller than 10 nm. The density of the nanostructures has been calculated to be about $2.5 \times 10^8 cm^{-2}$. Fig.1b shows the InP surface image after an Sb fluence of $1\times10^{12}ions/cm^2$. We observe that the nanostructures have become bigger in size. As seen in the size distribution of Fig. 2b, some structures have diameter as large as 1200nm. However, a large number of nanostructures have diameter smaller than 200nm. Although some nanostructures are as high as 18 nm, most of the nanostructures are lower than 12 nm (Fig. 3b). Furthermore, a large number of nanostructure have a height lower than 4 nm. The total density

of the nanostructures is found to be similar to that observed at $1\times10^{11}ions/cm^2$. At $1\times10^{13}ions/cm^2$, in Fig.1c, we notice a slight increase in the density of nanostructures to $3.6 \times 10^8 cm^{-2}$. A few nanostructures have diameters as large as 950 nm. A large number of nanostructures, greater than at $1\times10^{12}ions/cm^2$, have diameters smaller than 200 nm (Fig. 2c). Although some are 20 nm high, a large number have a height lower than 12 nm (Fig. 3c). Again, a large number of nanostructures have a height lower than 4 nm. The increase in density at this stage can also be noticed by a changed (y) scale for both the distributions. Fig. 1d shows the image acquired after the fluence of $1\times10^{14}ions/cm^2$. The density of the nanostructures is about $5.0 \times 10^8 cm^{-2}$. The size and the height distribution is very similar to that observed at $1\times10^{13}ions/cm^2$. However, the diameter of the largest nanostructures observed is smaller (700 nm) and the number of small (diameter less than 100 nm) nanostructures has increased (Fig. 2d). Also, larger number have a height lower than 4nm (Fig. 3d). After a fluence of $5 \times 10^{14} ions/cm^2$, a drastic increase in density of the nanostructures is observed in Fig. 1e. We also observe a larger number of nanostructure with small size. The density of nanostructures at this stage is about $8.0 \times 10^8 cm^{-2}$. Although the size distribution is similar to that observed at $1\times10^{14}ions/cm^2$, there are many more nano-structures with small 0-100 nm diameter (Fig. 2e). Similarly the nanostructures having height smaller than 4 nm has increased (Fig. 3e). The SPM image after a fluence of $1 \times 10^{15} ions/cm^2$ is shown in Fig. 1f. The density of the nanostructures, $8.0 \times 10^8 cm^{-2}$, as well as the size and the height distributions are very similar to those observed after $5 \times 10^{14} ions/cm^2$. However, some structures of large 1000 nm diameter (Fig. 2f) are also seen. Similar size and height distributions were also observed for $5\times10^{15}ions/cm^2$. Here we notice that for all fluences, the defect density is far lower than the ion beam fluence. Possible reasons for this will be discussed below.

Figure 4 shows the high resolution $1 \times 1 \mu m^2$, $0.5 \times 0.5 \mu m^2$ and $0.2 \times 0.2 \mu m^2$ images

of the InP(111) surfaces after the fluence of $1 \times 10^{13} ions/cm^2$ and $5 \times 10^{14} ions/cm^2$. The figures show that the InP(111) surfaces are very different, at each scale, for these two fluences. Some SPM -sections with images are shown in Fig. 5 to display some characteristic features of the distribution of the defects on InP surfaces. Fig. 5a shows a $1.0 \times 1.0 \mu m^2$ SPM image of InP surface after an ion fluence of $1 \times 10^{11} ions/cm^2$ along with the section analysis demonstrating a defect of 78.1 nm lateral and 1.8 nm vertical dimensions. Some defects of smaller size and height are also visible. Fig 5b shows $1.0 \times 1.0 \mu m^2$ SPM image of InP surface after an ion fluence of $1 \times 10^{12} ions/cm^2$. Some small and big sized defects are visible. Section analysis of a defect with dimensions 534 nm in lateral and 2.5 nm in vertical direction is also shown. We interestingly notice that this defect is actually composed of several smaller defects. These features can be clearly seen in Fig. 5c where a high resolution $0.4 \times 0.4 \mu m^2$ SPM image of this defect (from Fig. 5b) is shown. To emphasize, image in Fig. 5c shows the internal structure of the big defect analyzed in fig. 5b. As seen in Fig. 5c, the smaller defects embedded in the big defect are of several sizes and heights. Section-analysis of a typical small defect is shown in Fig.5c with dimensions of 34.0 nm in lateral and 1.0 nm in the vertical direction. The image also shows that several defects are overlapping other defects. To our knowledge, these kind of high resolution SPM images of the ion beam induced defects have never been reported in the literature. Fig. 5d shows a $1.0 \times 1.0 \mu m^2$ SPM image for a fluence of $1 \times 10^{13} ions/cm^2$. The section analysis shows a defect of 62.5 nm lateral and 4.9 nm vertical dimensions. Again, the big defects clearly appear to be composed of several smaller defects. Several small and lower defects can also be seen spread over the surface. Similar behaviour is also noticed in Fig.5e where a $1.0 \times 1.0 \mu m^2$ SPM image is shown for a fluence of $5 \times 10^{14} ions/cm^2$. The bigger defects are fully embedded with several smaller defects of various heights. The section analysis shows a defect with 46.9 nm lateral and 1.7 nm vertical dimensions. A big

defect is shown in a $0.5 \times 0.5 \mu m^2$ image of Fig.5f for a fluence of $1 \times 10^{15} ions/cm^2$. Here also the big defect is embedded with several smaller defects. The section analysis shows a defect with 27.0 nm lateral and 1.0 nm vertical dimensions. Several smaller defects can also be seen around the big defect. These images show that the bigger defects at all fluences are embedded with several of nanosized defects.

During the investigation of $10 \times 10 \mu m^2$ images of Fig.1, we had noticed that the density of defects for all fluences varies between $2.5\text{-}8.0\times10^8cm^{-2}$, which is much lower compared to the ion fluences. From fig. 5, we notice that the bigger defect structures are composed of smaller nanosized-defects of sizes ~ 30 nm. Taking this fact into account we have recalculated the density of defects and find it to be $5.0\times10^{10}cm^{-2}$ at $1\times10^{11}ions/cm^2$ and $1-1.5\times10^{11}cm^{-2}$ for higher fluences. We further notice, in Figs. 3 and 5, that the height of defects also vary as a function of fluence. Although, most of the defects are about 4 nm high, higher defects are also increasingly seen at larger fluences (see Fig. 3). In the framework of model introduced by Gibbons[22], the amorphous material is produced either directly by a single incoming ion or by multiple overlaps. According to this model, the ratio between the total surface area A_A covered by damages and the total area A_0 being implanted is given by

$$\frac{A_A}{A_0} = 1 - e^{-A_1 \phi} \sum_{k=0}^m \frac{(A_1 \phi)^k}{k!}$$

where $A_1 = \pi r_m^2$ is the surface area damaged by a single ion impact, ϕ is the fluence and m is the overlap number. For $1 \times 10^{11} ions/cm^2$ with r_m of 30 nm we find that m is 2, i.e. about two ions must impinge on the same area to produce the defect. For 250 MeV Xe irradiation of InP, Herre et al. find that the values of m is between 2 and 3 [23]. Higher heights of defects for larger fluences, as observed in Fig. 3, may denote larger m. In addition, more than one defect may be getting formed at one

place. Overlapping defects as well as defects smaller than 30 nm have also been seen in Fig. 5. All these factors together can be responsible for the observation of the lower defect density than the ion fluences.

We have also studied the rms surface roughness of the InP surfaces after MeV ion implantation. In Fig. 6 we have plotted the rms surface roughness(σ) of the InP surfaces as a function of ion fluence. For a virgin InP(111) surface, σ was measured to be 0.47 nm and is also marked in Fig. 6. We observe that the rms surface roughness exhibits two distinct behaviors as a function of fluence. Initially up to $1 \times 10^{14} ions/cm^2$, σ increases with the increasing fluence. However for higher fluences σ decreases for increasing fluences. Our results show that there is a critical fluence of $1 \times 10^{14} ions/cm^2$, below which the rms roughness of the InP surfaces increases with ion fluence whereas for higher fluences the surface roughness decreases with increasing fluences. A similar decrease in surface roughness with increasing fluence, beyond a critical fluence, has been observed for MeV Sb implantation in Si(100) [24] and for keV implantations of P and As in amorphous films [25]. Comparing results of 100 MeV Au SHI irradiation on InP (S_n = 378 eV/nm, S_e = 15 keV/nm) studies with our results (S_n = 2 keV/nm, $S_e = 1 \text{ keV/nm}$) we expect a higher surface rms roughness at all fluences here as the S_n is higher [12]. Although for fluences upto $1 \times 10^{13} ions/cm^2$ this is seen, for $1 \times 10^{14} ions/cm^2$ we observe a lower roughness in our case. This is an unexpected result and suggests that at higher fluences factors other than S_n are also playing role. At high fluences, density of electronic excitations increase, covalent bonds in the lattice weaken or get broken. As a result the lattice softens. This softening of the bonds and amorphization of the InP lattice has been shown by our Raman scattering results discussed below. The SHI studies [10] did not investigate the fluences higher than $1 \times 10^{14} ions/cm^2$ and also did not observe any decrease in the roughness. Our Raman scattering results, presented next, indicate the occurrence of amorphization

in InP at this fluence.

Fig. 7 shows the as-implanted Raman spectra from the InP samples implanted with various Sb doses. All these spectra were acquired in the backscattering geometry. The spectrum from a virgin (unimplanted) InP is also shown for comparison. The spectra have been shifted vertically for clarity, but the intensity scale is the same for all the spectra. The spectrum of the virgin InP (Fig.7) shows the characteristic longitudinal optical (LO) and transverse optical (TO) Raman peaks of crystalline InP(111) [26]. The features at 305 cm⁻¹ and at 347 cm⁻¹ are assigned to the TO and the LO phonon modes, respectively. The sequence of spectra gradually evolve, with increasing fluence, from the characteristic crystalline InP(111) spectrum to the amorphous like spectrum of Fig. 7f. The spectrum for the $1\times10^{11}ions/cm^2$ sample (Fig. 7a) exhibits some changes when compared to virgin InP. We observe that in addition to the shifts of both LO and TO features towards the lower wave numbers, TO feature also exhibits an asymmetric broadening towards the lower wave numbers. All these changes reflect the modifications in the InP due to the defects created during implantations. After a fluence $1 \times 10^{12} ions/cm^2$ (Fig. 7b) we observe a decrease in the intensity of the TO mode. In addition, broadening as well as the shifts towards lower wave numbers are observed, for both LO and TO modes. Spatial Correlation model related to q-vector relaxation induced damage shows [27] that when disorder is introduced into the crystal lattice by implantation, the correlation function of the phonon-vibrational modes becomes finite due to the induced defects and consequently the momentum q=0 selection rule is relaxed. Consequently, the phonon modes shift qualitatively to lower frequencies and broaden asymmetrically as the ion fluence is increased [28]. Thus the shifts to lower frequencies as well as the asymmetrical broadening of the features, observed in Fig. 7, are due to the residual defects created via implantation. Accordingly, these two features are also referred

to as DALO and DATO respectively for disorder activated (LO) and (TO) modes. The shifts, of the LO and TO modes, towards the lower wave numbers also indicate the development of the tensile strain in the lattice. Our results are in contrast to the studies of Si⁺ implantation in InP at 150 keV [17] where no noticeable changes compared to the virgin InP were seen upto the fluence of $1 \times 10^{12} ions/cm^2$ and the first signatures of disorder were observed after the fluence of $5 \times 10^{12} ions/cm^2$. For 2 MeV Se implantation in InP, however, some damage after $1 \times 10^{12} ions/cm^2$ has been reported using channeling experiments[29].

In Fig.7c after a fluence of $1\times10^{13}ions/cm^2$, a further decrease in the TO mode intensity as well as increased broadening and shifts of LO, TO modes towards smaller wave numbers are observed. After a fluence of $1\times10^{14}ions/cm^2$, the Raman spectrum (Fig. 7d) exhibits no distinct features corresponding to LO or the TO modes indicating that at this stage the lattice has been amorphised. The DATO and DALO structures have become completely merged into a broad band containing the whole density of states of the optical modes. This spectrum resembles that of amorphous InP [30]. Hence, we notice that InP has become amorphised at $1\times10^{14}ions/cm^2$ and further increase of fluences does not produce changes in the LO or TO modes (Fig. 7e, 7f). Since the penetration depth of Ar⁺ laser is 100 nm in InP, the Raman results here are primarily from surface region. The fluence, $1\times10^{14}ions/cm^2$, where InP becomes amorphised is surprisingly similar to that observed at keV energies [17, 31] or even at SHI energies [23]. The decrease in rms surface roughness, σ , (in Fig. 6) can thus be related to the amorphization of the InP at this fluence. The amorphization can lead to relaxations [32, 33] and smoothening of the surface via decreased strains [14].

There are some experimental observations on the nucleation and growth of defects formed by ion implantation in crystalline InP at keV [8] and at SHI [10, 21] energies. However, such studies are not present at MeV scales. The evolution of the surface

morphology during ion bombardment will be governed by a balance between the roughening and the smoothening processes. The random arrival of the ions on the surface constitutes the stochastic surface roughening. Surface diffusion, viscous flow and surface sputtering etc. contribute towards the smoothening of the surface [34]. The mechanism for the formation of surface damage is also postulated as a result of cascade collisions due to nuclear energy loss. S_n has been considered to be mainly responsible for the surface modifications of InP after 2 MeV Se implantation [29] and high energy ($\sim 100 \text{ MeV}$) Au irradiation [10]. In the present study also S_n seems to be the dominating factor in the creation of the nanostructure after Sb implantation. The 4.5 MeV Au implantation in HOPG [20] results in protrusions and features similar to the nanostructures seen here on InP surfaces. The mechanism for the formation of the surface features, on HOPG, was also S_n dominated. The nano-sized structures observed here, after MeV implantation, are smaller in size compared to structures seen after 2 keV Ar irradiation on InP surfaces where size ranged between 30-60 nm. Moreover, the height of the structures was over 100 nm after keV irradiation whereas it is always lower than 18 nm, and mostly around 4 nm, in the present case. Differential sputtering of InP surfaces leading to In-rich zones was suggested to be a possibility for the nucleation of surface structures after keV irradiation [8]. Similar scenario may be taking place at MeV energies also. Thus, S_n related processes, differential sputtering of a component, and the presence of tensile stress as observed in Raman spectra by softening of LO, TO modes, may be all together responsible for creating the nano-sized defects observed here after MeV Sb implantations.

4 Summary and conclusions

In the present study, the modifications in the surface morphology of InP(111) have been examined after 1.5 MeV Sb implantation. The InP surfaces display nano-sized defect structures. The height and size distributions of the nanostructures have been studied here. For fluences of 1×10^{12} - $1\times10^{15}ions/cm^2$, several nanostructures of sizes smaller than 100 nm and lower than 4 nm have been observed. Larger and bigger defects are observed to be embedded with smaller nano-sized defects in the SPM images. The surface roughness initially increases upto the Sb fluence of $1\times10^{14}ions/cm^2$. For higher fluences a decrease in surface roughness is observed. Raman Scattering results indicate that InP becomes amorphous at this stage. The decrease in surface roughness is related to the smoothening of surface due to amorphization. Nuclear energy loss processes and the presence of tensile stress, as shown by the softening of LO,TO modes by Raman scattering, may be together responsible for the formation of the nanoscale defect structures on the InP surfaces.

5 Acknowledgments

This work is partly supported by ONR grant no. N00014-97-1-0991. We would like the thanks N.C. Mishra for useful discussions.

References

- [1] D. Streit, Compound Semiconductors, May 2002.
- [2] B. Humphreys, A. O'Donell, Compound Semiconductors, August 2003.
- [3] D. Lammers, Electronic Engineering Times, 12 September 2002.
- [4] G. Tempel, N. Schwarz, F. Muller, F. Koch, H.P. Zeindl, and I. Eisele, Thin Solid Films 174 (1990) 171.
- [5] M.Tamura and T. Suzuki, Nucl. Instr. and Meth. **B39** (1989) 318.
- [6] G. Carter, M.J. Nobes, I.V. Katardjiev and J.L. Whitton Defect and Diffusion Forum, vol.57/58 (1988) 97-126. Ion Implantation 1988, ed. F.H. Wohlbier (Trans. Techn. Publ. Ltd).
- [7] D.J. DiMaria and D.R. Kerr, Appl. Phys. Lett. **27** (1975) 505.
- [8] Y. Yuba, S. Hazama, and K. Gamo, Nucl. Instru. Meth. B, **206** (2003) 648.
- [9] A. Kamarou, W. Wesch, E. Wendler, and S. Klaumunzer, Nucl. Instru. Meth. B, 225 (2004) 129.
- [10] J.P. Singh, R. Singh, N.C. Mishra, D. Kanjilal, and V. Ganeshan, Jour. Appl. Phys. 90 (2001) 5968.
- [11] W. K. Chu, J. W. Mayer and M. A. Nicolet, Backscattering Spectrometry (Academic Press, New York, 1978).
- [12] G.K. Mehta, Vacuum 48 (1997) 957.
- [13] S. Dey, G. Kuri, B. Rout and S. Varma, Nucl. Instr. Meth. B **142** (1998) 35.
- [14] S. Dey, C. Roy, A. Pradhan and S. Varma, J. Appl. Phys. 87 (2000) 1110.

- [15] X.Huang, F.Ninio, L.J.Brown and S.Prawer, J. Appl. Phys. 77 (1995) 5910.
- [16] X.Huang J. Phys. D: Appl. Phys. 28, 202 (1995).
- [17] R.Cusco, G.Talamas, and L. Artus, J.M. Martin and G. Gonzalez-Diaz, J. Appl. Phys 79 (1996) 3927.
- [18] H. Katsumata, S. Uekusa, H. Sai, M. Kumagai, Jour. Appl. Phys. 80 (1996) 2383.
- [19] J. P. Biersack and L. G. Haggmark, Nucl. Instr. and Meth. B174 (1980) 257.We have used the version SRIM'03
- [20] Y. Wang, Y. Kang, W. Zhao, S. Yan, P. Zhai and X. Tang J. Appl. Phys. 83 (1998) 1341.
- [21] J.P. Singh, R. Singh, N.C. Mishra, V. Ganeshan and D. Kanjilal, Nucl. Instru. B 179 (2001) 37.
- [22] J.F. Gibbons, Proc. IEEE **60** (1972) 1062.
- [23] O. Herre, W. Wesch, E. Wendler, P.I. Gaiduk. F.F. Komarov, S. Klaumunzer and P. Meier, Phy. Rev. B. 58 (1998) 4832.
- [24] S. Varma, S. Dey, V. Ganesan, submitted JAP.
- [25] R. Edrei, E.N. Shauly, A. Hoffman, J. Vac. Sci. Tech. A **20** (2002) 344.
- [26] A. Pinczuk, A.A. Ballman, R.E. Nahory, M.A. Pollack, and J.M. Worlock, J. Vac. Sci. Technol., 16 (1979) 1168.
- [27] K.K. Tiong, P.M. Amritharaj, F.H. Pollak and D.E. Aspens, Appl. Phys. Lett., 44, (1984) 122.

- [28] H. Richter, Z.P. Wang, L. Ley, Solid State Commun., 39 (1981) 625.
- [29] W. Wesch, E. Wendler, T. Bachmann, and O. Herre, Nucl. Instru. Meth. Res. B. 96 (1995)290.
- [30] M. Wihl, M. Cardona and J. Tauc, J. Non-Cryst. Solids 8-10 (1972) 172.
- [31] E.F. Kennedy, Appl. Phys. Lett, **38** (1981) 375.
- [32] C.A. Volkert, J. Appl. Phys. 70 (1991) 3521, and the references therein
- [33] P.C. Srivastava, V. Ganesan, O.P. Sinha, Nucl. Instru. Meth. in Phys. Res. B 222 (2004) 491.
- [34] E.A. Eklund, E.J. Snyder, and R.S. Williams, Surf. Sci. 285 (1993) 157.

Figures

Fig. 1: $10 \times 10 \mu m^2$ SPM images of InP surfaces for the virgin sample as well as after implantation with 1.5 MeV Sb ions at a fluence of (a) $1 \times 10^{11} ions/cm^2$, (b) $1 \times 10^{12} ions/cm^2$, (c) $1 \times 10^{13} ions/cm^2$, (d) $1 \times 10^{14} ions/cm^2$, (e) $5 \times 10^{14} ions/cm^2$. and (f) $1 \times 10^{15} ions/cm^2$

Fig. 2: Size distributions of the surface structures after 1.5 MeV Sb implantation with fluences of (a) $1 \times 10^{11} ions/cm^2$, (b) $1 \times 10^{12} ions/cm^2$, (c) $1 \times 10^{13} ions/cm^2$, (d) $1 \times 10^{14} ions/cm^2$, (e) $5 \times 10^{14} ions/cm^2$. and (f) $1 \times 10^{15} ions/cm^2$

Fig. 3: Height distributions of the surface structures after 1.5 MeV Sb implantation with fluences of (a) $1 \times 10^{11} ions/cm^2$, (b) $1 \times 10^{12} ions/cm^2$, (c) $1 \times 10^{13} ions/cm^2$, (d) $1 \times 10^{14} ions/cm^2$, (e) $5 \times 10^{14} ions/cm^2$. and (f) $1 \times 10^{15} ions/cm^2$

Fig. 4: InP surface SPM images (a) $1 \times 1\mu m^2$, (b) $0.5 \times 0.5\mu m^2$ and (c) $0.2 \times 0.2\mu m^2$ after implantation at fluence of $1 \times 10^{13} ions/cm^2$. Images (d) $1 \times 1\mu m^2$, (e) $0.5 \times 0.5\mu m^2$ and (f) $0.2 \times 0.2\mu m^2$ are after implantation at fluence of $5 \times 10^{14} ions/cm^2$.

Fig. 5: InP surface SPM images and SPM-section analysis of (a) $1 \times 1\mu m^2$ image for $1 \times 10^{11} ions/cm^2$ (b) $1.0 \times 1.0\mu m^2$ image for $1 \times 10^{12} ions/cm^2$ (c) $0.4 \times 0.4\mu m^2$ image for $1 \times 10^{12} ions/cm^2$ (d) $1 \times 1\mu m^2$ image for $1 \times 10^{13} ions/cm^2$ (e) $1 \times 1\mu m^2$ image for $5 \times 10^{14} ions/cm^2$ (f) $0.5 \times 0.5\mu m^2$ image for $1 \times 10^{15} ions/cm^2$. (L is the lateral dimension and H is the height of the nanostructure labelled with arrows)

Fig. 6: The rms surface roughness (σ) of the Sb implanted InP(111) surfaces, measured using SPM, is plotted as a function of Sb ion fluence. Data for the virgin sample

is also shown.

Fig. 7: Raman spectra are shown for virgin InP(111) as well as after 1.5 MeV Sb implantation of InP with various fluences of (a) 1×10^{11} , (b) 1×10^{12} , (c) 1×10^{13} (d) 1×10^{14} , (e) 5×10^{14} and (f) $1 \times 10^{15} ions/cm^2$. The curves are vertically displaced for clarity.

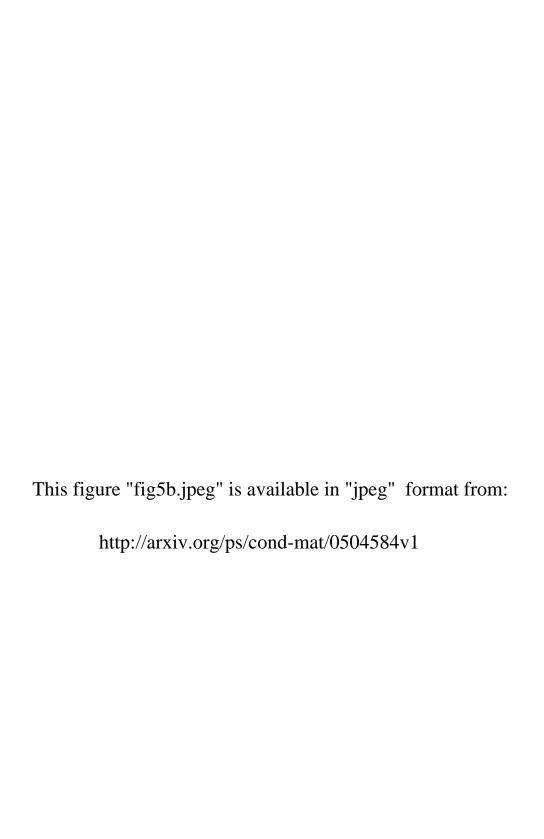
This figure "fig1.jpeg" is available in "jpeg" format from:

This figure "fig2.jpeg" is available in "jpeg" format from:

This figure "fig3.jpeg" is available in "jpeg" format from:

This figure "fig4.jpeg" is available in "jpeg" format from:

This figure "fig5a.jpeg" is available in "jpeg" format from: http://arxiv.org/ps/cond-mat/0504584v1



This figure "fig5c.jpeg" is available in "jpeg" format from:

This figure "fig6.jpeg" is available in "jpeg" format from:

This figure "fig7.jpeg" is available in "jpeg" format from: